Collision energy dependence of elliptic flow splitting between particles and their antiparticles from an extended multiphase transport model

Jun Xu[1] and Che Ming Ko[2]

[1]*Shanghai Institute of Applied Physics, Chinese Academy of Sciences, Shanghai 201800, China*
[2]*Cyclotron Institute and Department of Physics and Astronomy, Texas A&M University, College Station, Texas 77843, USA*

(Dated: March 9, 2022)

Based on an extended multiphase transport model, which includes mean-field potentials in both the partonic and hadronic phases, uses the mix-event coalescence, and respects charge conservation during the hadronic evolution, we have studied the collision energy dependence of the elliptic flow splitting between particles and their antiparticles. This extended transport model reproduces reasonably well the experimental data at lower collision energies but only describes qualitatively the elliptic flow splitting at higher beam energies. The present study thus indicates the existence of other mechanisms for the elliptic flow splitting besides the mean-field potentials and the need of further improvements of the multiphase transport model.

PACS numbers: 25.75.-q, 25.75.Ld, 25.75.Nq, 21.30.Fe, 24.10.Lx

I. INTRODUCTION

Understanding the phase diagram of quantum chromodynamics (QCD) is one of the main goals of heavy-ion collision experiments. From lattice QCD calculations, it is found that the hadron-quark phase transition is a smooth crossover at zero baryon chemical potential [1–3], corresponding to the matter at the top energy of relativistic heavy-ion collider (RHIC) and the large hadron collider (LHC). At finite baryon chemical potential as expected in lower collision energies, various theoretical models, e.g., the Nambu-Jona-Lasinio (NJL) model [4–7], have shown that the hadron-quark phase transition can be a first-order one. In order to search for the signal of the QCD critical point, which lies at the phase boundary between the smooth crossover transition to the first-order transition, great efforts have been made in several experimental programs. Among them, the Phase I of the beam-energy scan (BES) program has been carried out, and the Phase II of BES program as well as the compressed baryonic matter (CBM) program at the international Facility for Antiprotons and Ion Research (FAIR) are being planned.

The RHIC-BES I has led to many exciting findings, and among them the elliptic flow (v_2) splitting between particles and their antiparticles has attracted considerable theoretical attentions. For example, the v_2 splitting can be attributed to the larger v_2 for transported quarks than that for produced quarks, or similarly, their different rapidity dependencies [8–10], hydrodynamic evolution of the QGP at finite baryon chemical potential [11, 12], and the smaller radial flow of particles than their antiparticles [13]. The v_2 splitting between π^- and π^+ can also be attributed to the electric quadrupole moment in the produced quark-gluon plasma (QGP) due to the effect from the chiral magnetic wave [14] and their similar dynamics in the hadronic matter.

In our previous studies [15] by introducing mean-field potentials in both the partonic phase [16] and the hadronic phase [17] of a multiphase transport (AMPT) model, we reproduced the relative elliptic flow splitting between protons and antiprotons as well as kaons and antikaons at only the lowest energy of RHIC-BES, i.e., 7.7 GeV. Based on our previous models, we have made further modifications of the AMPT model in addition to the incorporation of the mean-field potential, such as applying the mix-event coalescence algorithm in the hadronization process and correcting the charge conservation in the hadronic phase. In the present study, we use this extended AMPT model to explore the collision energy dependence of elliptic flow splitting between particles and their antiparticles in heavy ion collisions.

This paper is organized as follows. In Sec. II, we review the partonic mean-field potentials based on a 3-flavor NJL model and the hadronic mean-field potentials from effective Lagrangians. The extensions made on the original AMPT model as well as the structure of the extended AMPT model are briefly described in Sec. III. The dynamics of produced baryon-rich matter and detailed results on the elliptic flow splitting between nucleons and antinucleons as well as that between K^+ and K^- at various collision energies are discussed in Sec. IV. In Sec.V, we summarize our results and discuss possible extensions of the present model and its applications.

II. MEAN-FIELD POTENTIALS

A. Partonic mean-field potentials

We first briefly review the mean-field potentials for particles and their antiparticles in the partonic and hadronic phase as used in our previous studies [15]. The partonic mean-field potentials in the baryon-rich quark matter are calculated from a 3-flavor NJL model [16] with

a Lagrangian given by [7]

$$\mathcal{L}_{\mathcal{NJL}} = \bar{q}(i\not{\partial} - M)q + \frac{G}{2}\sum_{a=0}^{8}\left[(\bar{q}\lambda^a q)^2 + (\bar{q}i\gamma_5\lambda^a q)^2\right] + \sum_{a=0}^{8}\left[\frac{G_V}{2}(\bar{q}\gamma_\mu\lambda^a q)^2 + \frac{G_A}{2}(\bar{q}\gamma_\mu\gamma_5\lambda^a q)^2\right] - K\left[\det{}_f\Big(\bar{q}(1+\gamma_5)q\Big) + \det{}_f\Big(\bar{q}(1-\gamma_5)q\Big)\right] \quad (1)$$

where $q = (u, d, s)^T$ is the quark field, $M = \mathrm{diag}(m_u, m_d, m_s)$ is the current quark mass matirx, and λ^a is the Gell-Mann matrices in $SU(3)$ flavor space with $\lambda^0 = \sqrt{2/3}I$. In the case that the vector and axial-vector interactions are generated by the Fierz transformation of the scalar and pseudo-scalar interactions, their coupling strengths are given by $G_V = G_A = G/2$, while $G_V = 1.1G$ was used in Ref. [18] to give a better description of the vector meson-mass spectrum based on the NJL model. The last term in Eq.(1), with the $\det_f$ denoting the determinant in the flavor space, is the Kobayashi-Maskawa-t'Hooft (KMT) interaction [19] that breaks the axial $U(1)_A$ symmetry.

In the mean-field approximation, the quark effective masses are given by

$$M_u = m_u - 2G\langle\bar{u}u\rangle + 2K\langle\bar{d}d\rangle\langle\bar{s}s\rangle = m_u + \Sigma_s^u, \quad (2)$$
$$M_d = m_d - 2G\langle\bar{d}d\rangle + 2K\langle\bar{s}s\rangle\langle\bar{u}u\rangle = m_d + \Sigma_s^d, \quad (3)$$
$$M_s = m_s - 2G\langle\bar{s}s\rangle + 2K\langle\bar{u}u\rangle\langle\bar{d}d\rangle = m_s + \Sigma_s^s, \quad (4)$$

where the quark condensate is

$$\langle\bar{q}_i q_i\rangle = -2M_i N_c\int\frac{d^3k}{(2\pi)^3 E_i}[1 - f_i(k) - \bar{f}_i(k)], \quad (i = u, d, s) \quad (5)$$

with the number of colors $N_c = 3$, the single-quark energy $E_i = \sqrt{M_i^2 + k^2}$, and $f_i(k)$ and $\bar{f}_i(k)$ being the phase-space distribution functions of quarks of flavor i and its anti-flavor, respectively. An iteration method is needed to calculate the effective mass M_i and the scalar potential Σ_s^i of flavor species i from Eqs. (2), (3), (4), and (5).

From the flavor-average treatment employed in Refs. [4, 20], the vector part in the Lagrangian is taken as $g_V\langle\bar{q}\gamma_\mu q\rangle^2$ with $g_V = (2/3)G_V$, and in this way the single-particle Hamiltonian of quark flavor i with momentum $\vec{p}$ is written as

$$H_i = \sqrt{M_i^2 + (\vec{p} \mp g_V\vec{\rho})^2} \pm g_V\rho^0, \quad (6)$$

where

$$\rho^\mu = 2N_c\sum_{i=u,d,s}\int\frac{d^3k}{(2\pi)^3 E_i}k^\mu[f_i(k) - \bar{f}_i(k)] \quad (7)$$

is the vector density with ρ^0 being its time component, i.e., the net quark density. As discussed in Ref. [16], the time component of the vector potential $\Sigma_v^0 = g_V\rho^0$ is more important than its space component in heavy ion collisions at 7.7 GeV. The reason is that the space component of the vector potential is related to the current that needs time to develop, while the elliptic flow is mostly produced at the early stage of the partonic phase.

As the NJL model is not renormalizable, the momentum integrations in Eqs. (5) and (7) require a cut-off momentum Λ. Taking $\Lambda = 750$ MeV [7, 18] and the current quark masses $m_u = m_d = 3.6$ MeV and $m_s = 87$ MeV, the values G and K can be determined from fitting the pion and kaon masses as well as the pion decay constant, and their values are $G\Lambda^2 = 3.6$ and $K\Lambda^5 = 8.9$ [7, 18]. Although the dynamics of partonic matter is treated relativistically in transport simulations, it is instructive to show the non-relativistic reduction of the mean-field potential $U_{q_i,\bar{q}_i} = \Sigma_s^i \pm \Sigma_v^0 - M_c^i$, where M_c^i is the constituent quark mass in vacuum. As an illustration, this potential is shown in panel (a) of Fig. 1 for u and $\bar{u}$ as well as in panel (b) of Fig. 1 for s and $\bar{s}$ in a quark matter with equal density for u, d, and s quarks at zero temperature for the cases of $R_V = G_V/G = 0$, 0.5, and 1.1. The mean-field potentials for d and $\bar{d}$ are exactly the same as those for u and $\bar{u}$ as we have not included isovector coupling in the NJL model. Although the scalar potential Σ_s^i for both quarks and antiquarks is attractive after subtracting M_c^i (see the curve with $R_V = 0$), the vector potential is repulsive for quarks and attractive for antiquarks, and this makes the potential for antiquarks more attractive than that for quarks. As seen in Fig. 1, the potential difference between quarks and antiquarks increases with increasing quark density ρ_q and increasing value of R_V. Because of the sufficiently large value of Λ used in our study, results presented in the following are not expected to be sensitive to its exact value.

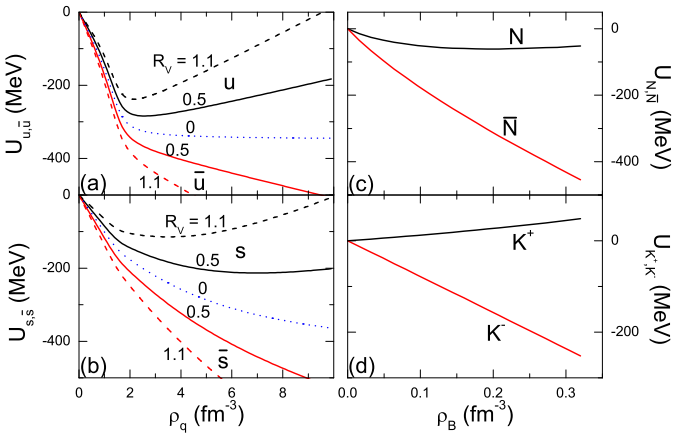

FIG. 1: (Color online) Reduced non-relativistic mean-field potentials for up quarks and anti-up quarks (a), strange quarks and anti-strange quarks (b), nucleons and antinucleons (c), and K^+ and K^- (d) in the cold antiquark- or antibaryon-free nuclear medium.

B. Hadronic mean-field potentials

For the nucleon and antinucleon potentials, we use those from the relativistic mean-field theory based on the following Lagrangian [21]:

$$\begin{aligned}\mathcal{L}_{\mathcal{H}} &= \overline{\psi}[i\gamma_\mu\partial^\mu - m - g_\sigma\sigma - g_\omega\gamma_\mu\omega^\mu]\psi + \frac{1}{2}(\partial^\mu\sigma)^2 \\ &- \frac{1}{2}m_\sigma^2\sigma^2 - \frac{1}{2}b\sigma^3 - \frac{1}{4}c\sigma^4 - \frac{1}{4}(\partial_\mu\omega^\nu - \partial_\nu\omega^\mu)^2 \\ &+ \frac{1}{2}m_\omega^2\omega^{\mu 2}, \end{aligned} \tag{8}$$

where ψ is the nucleon field with mass m, and σ and ω are the scalar and vector meson fields with masses m_σ and m_ω, respectively. The nucleon effective mass $m^\star$ and the kinetic momentum $p_\mu^\star$ are defined by

$$m^\star = m - \Sigma_s, \tag{9}$$
$$p_\mu^\star = p_\mu - \Sigma_{v\mu}, \tag{10}$$

where the nucleon scalar and vector self-energies are given, respectively, by

$$\Sigma_s = g_\sigma\langle\sigma\rangle, \tag{11}$$
$$\Sigma_{v\mu} = g_\omega\langle\omega_\mu\rangle. \tag{12}$$

In the mean-field approximation, the expectation values of the scalar and vector fields in nuclear medium are related to the nuclear scalar density ρ_s and current density ρ_μ via

$$m_\sigma\langle\sigma\rangle + b\langle\sigma\rangle^2 + c\langle\sigma\rangle^3 = g_\sigma\rho_s, \tag{13}$$
$$\langle\omega_\mu\rangle = (g_\omega/m_\omega^2)\rho_\mu. \tag{14}$$

In the local-density approximation, the scalar and vector densities can be further expressed in terms of the phase-space distribution functions $f(r,p^\star)$ of nucleons and $\bar{f}(r,p^\star)$ of antinucleons as

$$\rho_s = 4\int\frac{d^3p^\star}{(2\pi)^3}\frac{m^\star}{E^\star}[f(r,p^\star) + \bar{f}(r,p^\star)], \tag{15}$$
$$\rho_\mu = 4\int\frac{d^3p^\star}{(2\pi)^3}\frac{p_\mu^\star}{E^\star}[f(r,p^\star) - \bar{f}(r,p^\star)], \tag{16}$$

respectively, where $E^\star = \sqrt{m^{\star 2} + p^{\star 2}}$ is the single-particle energy. The time component of the vector density is thus exactly the net nucleon density. The scalar self-energy can be calculated self-consistently from Eqs. (9), (11), (13), and (15) using the iteration method. The parameters for a soft equation of state are used in the present study [21], i.e., $(g_\sigma/m_\sigma)m = 13.95$, $(g_\omega/m_\omega)m = 8.498$, $b/(g_\sigma^3 m) = 0.0199$, and $c/g_\sigma^4 = -0.00296$.

Based on the G-parity invariance, the non-relativistic reduction of the potentials for nucleons and antinucleons are

$$U_{N,\bar{N}} = -\Sigma_s \pm \Sigma_v^0, \tag{17}$$

where Σ_v^0 is the time component of the vector potential, and the '+' and '−' signs are for nucleons and antinucleons, respectively. As an illustration, we show in panel (c) of Fig. 1 the potentials for nucleons and antinucleons at zero temperature in antibaryon-free hadronic matter. It is seen that the potential for nucleons is slightly attractive, while that for antinucleons is deeply attractive, with the former about −60 MeV and the latter about −260 MeV at the saturation density $\rho_0 = 0.16$ fm^{-3}. In the hadronic matter with strange baryons and baryon resonances, the phase-space distribution functions $f(r,p^\star)$ and $\bar{f}(r,p^\star)$ are calculated from all the baryons and antibaryons according to their light quark content.

For the kaon and antikaon potentials in nuclear medium, they are obtained from the chiral effective Lagrangian [22], that is, $U_{K,\bar{K}} = \omega_{K,\bar{K}} - \omega_0$ with

$$\omega_{K,\bar{K}} = \sqrt{m_K^2 + p^2 - a_{K,\bar{K}}\rho_s + (b_K\rho_B^{\rm net})^2} \pm b_K\rho_B^{\rm net} \tag{18}$$

and $\omega_0 = \sqrt{m_K^2 + p^2}$, where $m_K = 498$ MeV is the kaon mass, and the values of other parameters are set as $a_K = 0.22$ GeV^{2}fm^3, $a_{\bar{K}} = 0.45$ GeV^{2}fm^3, and $b_K = 0.333$ GeVfm^3 [22]. In the above, ρ_s is the scalar density determined from the effective Lagrangian in Eq. (8), and $\rho_B^{\rm net} = \rho_B - \rho_{\bar{B}}$ is the net baryon density. The "+" and "−" signs are for kaons and antikaons, respectively. The potentials for K^+ and K^- at rest in nuclear matter at zero temperature are displayed in panel (d) of Fig. 1. The potential for K^+ is seen to be slightly repulsive while that for K^- is deeply attractive, with the former about 20 MeV and the latter about −125 MeV at the saturation density.

We have also introduced the s-wave pion potentials in the hadronic phase as in Ref. [17]. In the absence of the isovector coupling in the partonic phase, it has been shown that the v_2 splitting of π^- and π^+ due to their potentials in the hadronic phase has the correct sign compared with the experimental data but the magnitude is much smaller. In the present study, we thus only discuss the v_2 splitting between nucleons as well as kaons and their antiparticles, and postpone the study of the effects of isovector mean fields in relativistic heavy-ion collisions.

III. THE EXTENDED AMPT MODEL

To include the mean-field potentials for both partons and hadrons in relativistic heavy-ion collisions, we have made extensive modifications to the string melting version of the AMPT model [23–25]. The original string melting version has been successfully used to describe the charge particle multiplicity, the collective flow, and the dihadron correlations in heavy-ion collisions at the top energies at RHIC and LHC [26–29], where the mean-field potentials for particles and their antiparticles are not included in either the partonic phase or the hadronic phase as their effects are less important than partonic and

hadronic scatterings on the collision dynamics. However, the mean-field effects become non-negligible in heavy-ion collisions at energies of the RHIC-BES program and the future FAIR-CBM program. In the following, we briefly discuss the extended AMPT model used in the present study.

The initial condition of the AMPT model is obtained from the heavy-ion jet interaction generator (HIJING) model [30], where both soft and hard parton production are included by using the Monte Carlo Glauber model with shadowing effects included for nucleus-nucleus collisions. In the original string melting version, which converts hadrons produced from initial collisions into their valence quarks and antiquarks, the interaction in the partonic phase is described only by parton-parton elastic scatterings based on Zhang's parton cascade (ZPC) model [31] without mean-field potentials for partons. In the present study as well as those reported in Refs. [15, 16], the ZPC model is replaced by a 3-flavor NJL transport model that includes both scalar and vector potentials for partons as well as the parton elastic scattering process. To calculate the mean-field potentials, the test-particle method [32] with parallel events for the same impact parameter is used. For the parton scattering cross section, it can in principle be obtained also from the NJL model [33]. In this case, the parton scattering cross section would depend on the temperature and quark chemical potential of the partonic matter. Since it is essential for our model to reproduce the experimentally measured charged particle elliptic flow before addressing the effect of mean-field potentials on the elliptical flow splitting between particles and their antiparticles, we take the value of the scattering cross section between partons in the same event as a parameter and determine its value by fitting the experimental charged particle elliptic flow, as will be shown in the next section.

The partonic evolution ends when the chiral phase transition happens, i.e., the effective mass of light quarks in central cells of the system is half of that in vacuum. A spatial coalescence model as used in the original AMPT model is then used to describe the hadronization process with the hadron species determined by the flavor and invariant mass of its constituent quarks or antiquarks. However, instead of coalescence of quarks in the same event, we extend the coalescence algorithm to allow quarks and antiquarks in an event to coalesce with those in other parallel events. The hadronization treatment of completely mixing the quarks and antiquarks from all parallel events is equivalent to the use of smooth quark and antiquark phase-space distributions for hadron production via quark coalescence in the pioneering studies in Refs. [34–37], and is particularly useful for rare antiparticles produced at lower collision energies. To keep the fluctuation in the number of hadrons produced from these parallel events, we allow, however, quarks and antiquarks in a given event to coalesce only with certain quarks and antiquarks in the parallel events so that the numbers of mesons and baryons produced in each event are the same as in the original AMPT model. This is possible because in the string melting version of AMPT, partons in each event are obtained from converting the baryons and mesons produced from HIJING into its constituents, and daughter partons from the same hadron are labeled. In the coalescence algorithm for the hadronization of the partonic matter after its evolution, a parton recombines with other partons that are the closest in coordinate space. If the latter are originally from a different hadron, the sibling partons associated with the hadronized parton are then relabeled as the siblings of the parton whose siblings are involved in this particular coalescence. Allowing parton relabelings between parallel events thus does not alter the number of hadrons produced in a given event even the coalescence is done with mixed events. We note that although the event-by-event particle number fluctuation is maintained in the mixed-event coalescence method, the event-by-event density fluctuation is largely averaged out by using partons from parallel events to evaluate the mean-field potentials. The only remaining density fluctuation effect comes from the parton scatterings because only partons in the same event can scatter in this extended AMPT model.

After hadronization, a relativistic transport (ART) model is used to describe the evolution of the hadronic phase [38], in which both particle-antiparticle annihilations and their inverse processes are included. The mean-field potentials for hadrons in the ART model are also turned on [17] by using the test-particle method with parallel events. Since charges are not strictly conserved in some of the inelastic processes in the original ART model, we have corrected this problem by resampling the inelastic channels until the charge is conserved.

IV. RESULTS AND DISCUSSIONS

Based on the above extended AMPT model, we have studied heavy-ion collisions at RHIC-BES energies. Here, we focus on the evolution of the baryon-rich matter produced in these collisions, and discuss the difference in the elliptic flows between particles and their antiparticles.

A. Charged particle elliptic flow

We first assume that the parton scattering cross section in the NJL transport model is isotropic and determine its value by fitting the final charged particle elliptic flow to the experimental data. As displayed in Fig. 2, the parton scattering cross sections of 1 mb for 7.7 GeV, 3 mb for 11.5 GeV, 5 mb for 19.6 GeV, 8 mb for 27 GeV, and 10 mb for 39 GeV can reproduce reasonably well the transverse momentum dependence of the elliptic flow of mid-pseudorapidity particles, by using the same sub-$|\eta|$ method as applied in the experimental analysis [39]. The reason why a larger cross section is needed at higher energies is due to the attractive scalar partonic potential

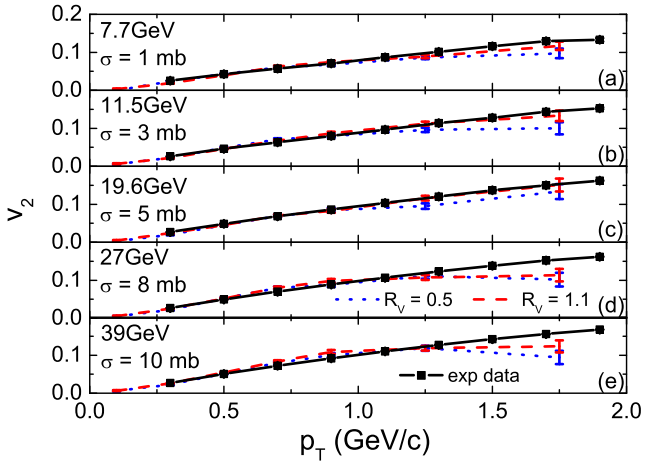

FIG. 2: (Color online) Differential elliptic flow of mid-pseudorapidity ($|\eta| < 1$) particles in mid-central ($20 - 30\%$) Au+Au collisions at $\sqrt{s_{NN}} = 7.7$ (a), 11.5 (b), 19.6 (c), 27 (d), and 39 GeV (e) with different values of R_V. The experimental data are taken from Ref. [39].

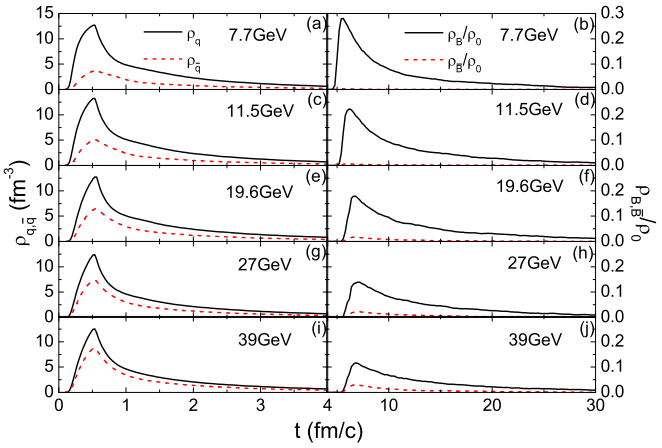

FIG. 3: (Color online) Time evolution of densities of quarks and antiquarks (left columns) as well as baryons and antibaryons (right columns) in central cells of the partonic and the hadronic phase, respectively, in mid-central ($20 - 30\%$) Au+Au collisions at $\sqrt{s_{NN}} = 7.7$, 11.5, 19.6, 27, and 39 GeV.

in the NJL transport model, whose effect is more pronounced at higher collision energies. However, the larger parton scattering cross section at higher beam energies likely leads to a decreasing specific shear viscosity η/s of the partonic matter, i.e., the ratio of the shear viscosity η to the entropy density s, with increasing temperature, contrary to results from other studies (see, e.g., Ref. [40]). This is because $\eta \sim \langle p \rangle/\sigma$ with the average momentum $\langle p \rangle$ proportional to the temperature T according to Ref. [27] and $s \sim T^3$ if we assume that the partonic matter consists of non-interacting massless up and down quarks, so $\eta/s \sim 1/(T^2\sigma)$ decreases with temperature. To obtain a more realistic behavior for the η/s, such as that from the NJL model [33, 41], requires an improved calculation using a parton scattering cross section that depends on the local temperature and density [27, 42]. Such a study is, however, beyond the scope of the present study. Figure 2 further shows that reducing the strength of the vector potential in the partonic phase by a factor of two only slightly lowers the elliptic flow. Therefore, once the parton scattering cross section is fitted, the relative contributions from the partonic and hadronic phases to the elliptic flows are well constrained.

B. Density evolution

We display in Fig. 3 the time evolution of particle and antiparticle densities in the baryon-rich matter produced in mid-central ($20 - 30\%$) Au+Au collisions at $\sqrt{s_{NN}} = 7.7$, 11.5, 19.6, 27, and 39 GeV. In the partonic phase, it is seen that the peak quark density in central cells is similar at different collision energies, although the lifetime of the partonic phase is generally longer at higher collision energies. However, the antiquark density in central cells increases with increasing beam energy as a result of higher temperatures and smaller quark chemical potentials reached at higher collision energies. In the hadronic phase, the baryon density in central cells is higher at lower collision energies compared to that at higher collision energies, while this is the other way round for the antibaryon density. The later appearance of hadrons at higher collision energies is due to the later freeze-out of the partonic phase and the additional hadron formation time of 0.7 fm/c introduced in the AMPT model. It is also seen that based on the present hadronization condition, the density in the hadronic phase is much smaller than the saturation density ρ_0.

C. Elliptic flow splitting

Figure 4 displays the v_2 difference between light quarks as well as strange quarks and their antiquarks after the partonic evolution at various collision energies. As expected, the v_2 difference between quarks and their antiquarks generally increases with increasing strength of the vector potential denoted as R_V, although at higher collision energies it is not so sensitive to R_V and is much smaller. This is understandable since the difference between the densities of quarks and antiquarks becomes smaller at higher beam energies as shown in Fig. 3. In addition, the v_2 splitting comes mainly from the time component of the vector potential, while the space component of the vector potential, which contributes oppositely to the v_2 splitting, becomes more important at higher collision energies.

As mentioned and shown in Refs. [15, 16], the initial nucleons in the hadronic phase formed from light quarks have a larger v_2 than antinucleons formed from light

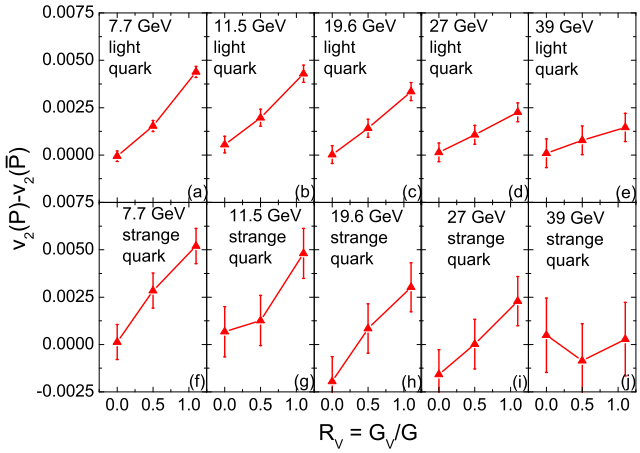

FIG. 4: (Color online) The elliptic flow difference between mid-rapidity light quarks and their antiquarks (upper panels) as well as that between mid-rapidity strange quarks and anti-strange quarks (lower panels) at the end of the partonic phase in mini-bias (0−80%) Au+Au collisions at $\sqrt{s_{NN}}$ = 7.7, 11.5, 19.6, 27, and 39 GeV, with R_V = 0, 0.5, and 1.1.

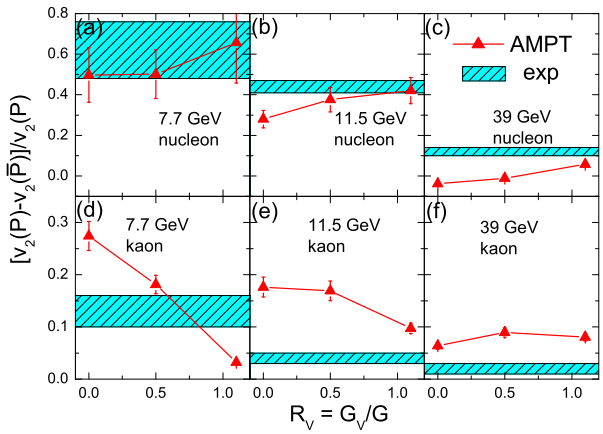

FIG. 5: (Color online) The relative elliptic flow difference between mid-rapidity nucleons and antinucleons (upper panels) and that between mid-rapidity K^+ and K^- (lower panels) in the final stage of mini-bias (0 − 80%) Au+Au collisions at $\sqrt{s_{NN}}$ = 7.7, 11.5, and 39 GeV, with R_V = 0, 0.5, and 1.1, and experimental data from Ref. [43].

antiquarks. For the initial K^+ in the hadronic phase, formed from a light quark and a strange antiquark, their v_2 is smaller than K^- formed from a light antiquark and a strange quark, since strange quarks (antiquarks) are heavier than light quarks (antiquarks) and thus contribute more to the v_2 of produced kaons.

The relative v_2 difference, i.e., v_2 difference divided by v_2 of positively charged particles, between final nucleons and antinucleons as well as that between final K^+ and K^- at $\sqrt{s_{NN}}$ = 7.7, 11.5, and 39 GeV are shown in Fig. 5. Qualitatively, the relative v_2 difference between nucleons and antinucleons increases with increasing R_V, while that between K^+ and K^- mostly decreases with increasing R_V. In order to reproduce the relative v_2 difference data from Ref. [43] at 7.7 GeV, R_V is constrained between 0.5 and 1.1 by taking results from both nucleons and kaons into consideration, consistent with the conclusion in Ref. [15]. At 11.5 GeV, it seems that an even larger value of R_V is needed to reproduce the experimental relative v_2 difference. At 39 GeV, the results are, however, not so sensitive to the strength of the vector potential, and our results underestimate the relative v_2 difference between nucleons and antinucleons but overestimate that between K^+ and K^-, although the energy dependence is qualitatively consistent with the experimental data.

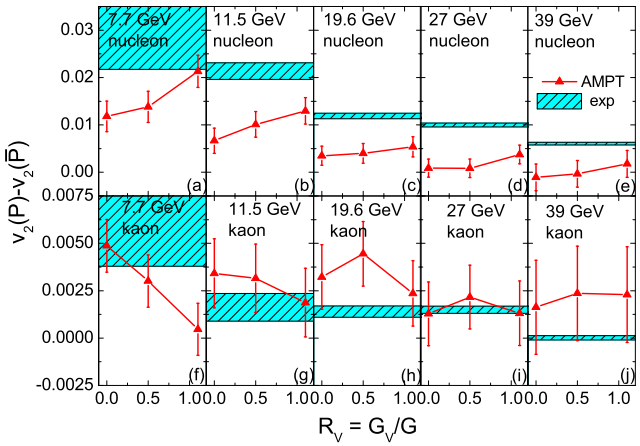

FIG. 6: (Color online) The elliptic flow difference between mid-rapidity nucleons and antinucleons (upper panels) as well as that between mid-rapidity K^+ and K^- (lower panels) in the final stage of mini-bias (0 − 80%) Au+Au collisions at $\sqrt{s_{NN}}$ = 7.7, 11.5, 19.6, 27, and 39 GeV, with R_V = 0, 0.5, and 1.1, and experimental data from Ref. [44].

In Fig. 6, the absolute v_2 difference between nucleons and antinucleons as well as K^+ and K^- are compared with experimental results from Ref. [44] at various collision energies. The absolute v_2 difference raises more challenges to the model than the relative v_2 difference, since this requires to reproduce the v_2 of various particle species as well. At lower collision energies, the v_2 difference between nucleons and antinucleons increases with increasing R_V, and that between K^+ and K^- decreases with increasing R_V. At 7.7 GeV, the v_2 difference between nucleons and antinucleons favors R_V = 1.1, while that between K^+ and K^- favors values of R_V between 0 and 0.5. At higher collision energies, although our model gives qualitatively the correct sign as well as the energy dependence of the v_2 splitting, it underestimates the v_2 difference between nucleons and antinucleons but reproduces that between K^+ and K^- within the statistical error.

V. CONCLUSIONS AND OUTLOOK

Based on an extended AMPT model, which includes mean-field potentials in both the partonic and the hadronic phase, uses the mix-event coalescence for hadronization, and ensures the charge conservation during the hadronic evolution, we have studied the energy dependence of elliptic flow splitting between particles and their antiparticles at RHIC-BES energies. The density evolutions of particles and their antiparticles in both the partonic and hadronic phases are illustrated. The elliptic flow splitting from the contribution of the partonic phase and the further modification in the hadronic phase at various collision energies is observed. Our model can describe reasonably well the elliptic flow splitting at lower collision energies, and can describe qualitatively but not quantitatively that at higher beam energies. Especially, our model underestimates the elliptic flow splitting between nucleons and antinucleons at higher collision energies. The present study thus calls for other mechanisms in addition to the mean-field potentials that may contribute to the elliptic flow splitting between particles and their antiparticles.

The present model can be further improved in several ways for a better description of the collision dynamics at RHIC-BES energies. First, the yield ratio of baryon/antibaryon from the present AMPT model is different from that obtained experimentally, or that based on the baryon chemical potential and temperature at chemical freeze-out from fitting the experimental data using the thermodynamical model. This could be improved by modifying the initial parton species or the coalescence algorithm [45]. Second, the mixing and interaction between the partonic phase and the hadronic phase are still missing in our model, but they could be important in heavy-ion collisions at RHIC-BES energies. Third, the annihilation process for baryons and antibaryons could be overestimated in the model, as the elliptic flow difference between nucleons and antinucleons can be increased by reducing the annihilation effect. Fourth, it is of interest to include the isovector coupling [46] in the NJL transport model and the symmetry energy effect in the hadronic phase, as this would allow us to study, respectively, the elliptic flow difference between π^+ and π^- and the interesting isospin dynamics in heavy ion collisions at the RHIC-BES and FAIR-CBM energies.

Acknowledgments

We thank Nu Xu for the suggestion of carrying out this study, Chen Zhong for maintaining the high-quality performance of the computer facility, Lie-Wen Chen for helpful comments, and Lilin Zhu for the hospitality at Sichuan University. The work of JX was supported by the Major State Basic Research Development Program (973 Program) of China under Contract Nos. 2015CB856904 and 2014CB845401, the National Natural Science Foundation of China under Grant Nos. 11475243 and 11421505, the "100-talent plan" of Shanghai Institute of Applied Physics under Grant Nos. Y290061011 and Y526011011 from the Chinese Academy of Sciences, the Shanghai Key Laboratory of Particle Physics and Cosmology under Grant No. 15DZ2272100, and the "Shanghai Pujiang Program" under Grant No. 13PJ1410600, while that of CMK was supported by the US Department of Energy under Contract No. DE-SC0015266 and the Welch Foundation under Grant No. A-1358.

[1] C. Bernard, T. Burch, C. Detar *et al.*, Phys. Rev. D **71**, 034504 (2005).
[2] Y. Aoki, G. Endrodi, Z. Fodor *et al.*, Nature **443**, 675 (2006).
[3] A. Bazavov, T. Bhattacharya, T. Cheng *et al.*, Phys. Rev. D **85**, 054503 (2012).
[4] M. Asakawa and K. Yazaki, Nucl. Phys. A **504**, 668 (1989).
[5] K. Fukushima, Phys. Rev. D **77**, 114028 (2008) [Erratumibid. D **78**, 039902 (2008)].
[6] S. Carignano, D. Nickel, and M. Buballa, Phys. Rev. D **82**, 054009 (2010).
[7] N. M. Bratovic, T. Hatsuda, and W. Weise, Phys. Lett. B **719**, 131 (2013).
[8] J. C. Dunlop, M. A. Lisa, and P. Sorensen, Phys. Rev.C **84**, 044914 (2011).
[9] V. Greco, M. Mitrovski, and G. Torrieri, Phys. Rev. C **86**, 044905 (2012).
[10] Yu. B. Ivanov, Phys. Lett. B **723**, 475 (2013).
[11] J. Steinheimer, V. Koch, and M. Bleicher, Phys. Rev. C **86**, 044903 (2012).
[12] Y. Hatta, A. Monnai, and B. W. Xiao, Phys. Rev. D **92**, 114010 (2015).
[13] X. Sun, H. Masui, A. M. Poskanzer, and A. Schmah, Phys. Rev. C **91**, 024903 (2015).
[14] Y. Burnier, D. E. Kharzeev, J. Liao, and H. U. Yee, Phys. Rev. Lett. **107**, 052303 (2011).
[15] J. Xu, T. Song, C. M. Ko, and F. Li, Phys. Rev. Lett. **112**, 012301 (2014).
[16] T. Song, S. Plumari, V. Greco, C. M. Ko, and F. Li, arXiv:1211.5511 [nucl-th].
[17] J. Xu, L. W. Chen, C. M. Ko, and Z. W. Lin, Phys. Rev. C **85**, 041901 (2012).
[18] M. F. M. Lutz, S. Klimt, and W. Weise, Nucl. Phys. A **542**, 521 (1992).
[19] G. 't Hooft, Phys. Rev. D **14**, 3432 (1976); **18**(E), 2199 (1978).
[20] T. Hatsuda and T. Kunihiro, Phys. Rept. **247**, 221 (1994).
[21] G. Q. Li, C. M. Ko, X. S. Fang, and Y. M. Zheng, Phys. Rev. C **49**, 1139 (1994).
[22] G. Q. Li, C. H. Lee, and G. E. Brown, Phys. Rev. Lett.

79, 5214 (1997); Nucl. Phys. A **625**, 372 (1997).
[23] Z. W. Lin, C. M. Ko, B. A. Li, B. Zhang, and S. Pal, Phys. Rev. C **72**, 064901 (2005).
[24] B. Zhang, C. M. Ko, B. A. Li, and Z. W. Lin, Phys. Rev. C **61**, 067901 (2000).
[25] Z. W. Lin and C. M. Ko, Phys. Rev. C **65**, 034904 (2002).
[26] J. Xu and C. M. Ko, Phys. Rev. C **83**, 021903 (R) (2011).
[27] J. Xu and C. M. Ko, Phys. Rev. C **83**, 034904 (2011).
[28] J. Xu and C. M. Ko, Phys. Rev. C **84**, 014903 (2011).
[29] J. Xu and C. M. Ko, Phys. Rev. C **84**, 044907 (2011).
[30] X. N. Wang and M. Gyulassy, Phys. Rev. D **44**, 3501 (1991).
[31] B. Zhang, Comp. Phys. Comm. **109**, 193 (1998).
[32] C. Y. Wong, Phys. Rev. C **25**, 1460 (1982).
[33] R. Marty, E. Bratkovskaya, W. Cassing, J. Aichelin, and H. Berrehrah, Phys. Rev. C **88**, 045203 (2013).
[34] V. Greco, C. M. Ko, and P. Levai, Phys. Rev. Lett. **90**, 202302 (2003).
[35] V. Greco, C. M. Ko, and P. Levai, Phys. Rev. C **68**, 034904 (2003).
[36] R. J. Fries, B. Muller, C. Nonaka, and S. A. Bass, Phys. Rev. Lett. **90**, 202303 (2003).
[37] R. C. Hwa and C. B. Yang, Phys. Rev. C **67**, 034902 (2003).
[38] B. A. Li and C. M. Ko, Phys. Rev. C **52**, 2037 (1995).
[39] L. Adamczyk *et al.* (STAR Collaboration), Phys. Rev. C **86**, 054908 (2012).
[40] N. Christiansen, M. Haas, J. M. Pawlowski, and N. Strodthoff, Phys. Rev. Lett. **115**, 112002 (2015).
[41] Sanjay K. Ghosh, Sibaji Raha, Rajarshi Ray, Kinkar Saha, and Sudipa Upadhaya, Phys. Rev. D **91**, 054005 (2015).
[42] M. Ruggieri, F. Scardina, S. Plumari, and V. Greco, Phys. Rev. C **89**, 054914 (2014).
[43] B. Mohanty (for STAR Collaboration), J. Phys. G **38**, 124023 (2011).
[44] L. Adamczyk *et al.* (STAR Collaboration), Phys. Rev. Lett. **110**, 142301 (2013).
[45] Z. W. Lin, private communications.
[46] H. Liu, J. Xu, L. W. Chen, and K. J. Sun, Phys. Rev. D **94**, 065032 (2016).